Reducing lead toxicity in the methylammonium lead halide MAPbI₃: Why Sn substitution should be preferred to Pb vacancy for optimum solar cell efficiency

Pooja Basera [●],[*] Manish Kumar [●], Shikha Saini [●], and Saswata Bhattacharya [●][†]
Department of Physics, Indian Institute of Technology Delhi, New Delhi 110016, India

Methylammonium lead halide (MAPbI₃) perovskite has emerged as one of the frontier optoelectronic semiconductors. To avoid lead toxicity, the role of Sn substitution and Pb vacancy (Pb-⊠) are addressed in regulating stability and solar cell efficiency of $MAPb_{1-X-Y}Sn_X⊠_YI_3$ perovskite using hybrid density functional theory (DFT). The role of spin-orbit coupling (SOC) and the electron's self-interaction error are examined carefully. We find to reduce the Pb content from pristine MAPbI₃, Sn substitution has a more favorable thermodynamic stability than creating Pb-⊠. Moreover, on substituting Sn, due to strong *s-p* and *p-p* couplings, the lower parts of the conduction band gets shifted downwards, which results in the reduction of the band gap (direct). This further helps us to get a high optical absorption coefficient (redshifted) and maximum solar cell efficiency in $MAPb_{1-X}Sn_XI_3$ for $0 < X \leqslant 0.5$.

I. INTRODUCTION

Inorganic-organic halide perovskite compounds with chemical formula ABX₃, in particular methylammonium lead halide (MAPbI₃), have drawn significant scientific interest in recent years [1–4]. Long diffusion length, high carrier mobility, suitable optical band gaps (1.55–1.69 eV) [1,5–7], strong absorption of light, and very cheap manufacturing costs have enabled its revolutionary success in the field of solid-state photovoltaics [2,8–12]. While the first experimental work turned power conversion efficiency (PCE) to be just 3.8% of sunlight energy into electricity [1], the efficiency of perovskite solar cells subsequently has been enhanced rapidly by adapting novel methodologies during the fabrication process [13–15]. Recently, a maximum PCE of 22.1% has been reported for MAPbI₃ under the operational condition [16]. Therefore, MAPbI₃ attracts a huge interest along with commercialized thin-film solar cells, e.g., silicon, GaAs, and CdTe [17].

However, the toxic nature of Pb has hindered MAPbI₃ from its practical applications. Also, when exposed to moisture and air, Pb is intrinsically unstable which eventually causes oxidation from Pb^{2+} to Pb^{4+}. This leads to degradation of photovoltaic performance [18,19]. Therefore, reducing the extent of Pb by substituting suitable alternatives (e.g., Sn, Ge, Sr, etc.) in the perovskite has been crucial. But, the complete removal of Pb from the perovskite cage degrades drastically the solar cell performance [20–22]. In view of this, there are a lot of reports on partial substitution of Pb with Sn by forming a hybrid perovskite $MAPb_{1-X}Sn_XI_3$ [12,20,23–25]. However, identification and hence controlling the effect of different defects [viz. Sn substitution or Pb vacancy (Pb-⊠)] is quite difficult and very much indirect

experimentally. This indeed is the reason behind several controversies between the experimentally and theoretically predicted structural parameters, formation energy of most stable defects, its concentration, and preferred charge state of $MAPb_{1-X}Sn_XI_3$ [26,27]. In addition to this, the issues related to the power conversion efficiency and how it correlates with the reduction of Pb content are also not well understood. Thus, despite several researchers having explored structural defects in pristine MAPbI₃ [10,20,25,28,29], there is justified importance to revisit this rigorously studied semiconducting material to provide theoretical guidance to experiment.

Understanding this at the theoretical (e.g., density functional theory (DFT) [30,31]) level has never been easy because of the exchange-correlation ϵ_{xc} functional that needs to be carefully analyzed in the light of the electron's self-interaction error and spin-orbit coupling (SOC) effect. Note that since they contribute counter to each other, there is a lucky cancellation of both for pristine MAPbI₃, which encourages researchers to use simple GGA (PBE) functionals for this system [32–35]. However, the whole motivation of this work is to examine the removal of Pb with Sn or vacancy. Since Sn is lighter than Pb, and the effect of SOC is smaller [36]. Therefore, a simple GGA functional can never give correct energetics to this composite system $MAPb_{1-X-Y}Sn_X⊠_YI_3$. In addition, the accurate determination of ground-state formation energy is still a debateful topic [37–39], where the role of self-interaction error and SOC need to be examined carefully.

In this paper, using state-of-the-art first-principles based methodology under the framework of DFT (with hybrid functionals [40] combined with SOC), we present an exhaustive study on the theoretical understanding of the structural defects to explore the role of Sn substitution and Pb-⊠ in regulating the thermodynamic stability of $MAPb_{1-X-Y}Sn_X⊠_Y I_3$ perovskite. First, the performance of DFT ϵ_{xc} functional (PBE/HSE06) [40,41] is carefully analyzed in the light of SOC effect. Then, from the formation energies of

*pooja.basera@physics.iitd.ac.in
†saswata@physics.iitd.ac.in

MAPb$_{1-X-Y}$Sn$_X$ ⊠$_Y$ I$_3$ conformers, the most stable ground-state configurations are identified. Furthermore, we have demonstrated the electronic structure to identify possible optical transitions. Subsequently, we have explored optical properties and spectroscopic limited maximum efficiency (SLME) for thermodynamically stable configurations to understand how the efficiency correlates with Sn substitution.

II. METHODOLOGY

The DFT calculations are performed with PAW pseudopotential method [42] as implemented in Vienna *ab initio* simulation package (VASP) [43]. The supercell size of the model structure of MAPb$_{1-X-Y}$Sn$_X$ ⊠$_Y$ I$_3$ [44] has been kept increasing until the single defect state becomes fully localized (2×2×2), consisting of 96 atoms (i.e., MA$_8$Pb$_8$I$_{24}$) with periodic boundary conditions. We have used exchange and correlation (xc) functionals viz. generalized gradient approximation (GGA with PBE) and hybrid functional HSE06 with and without SOC for the calculations. The atomic positions of the structures are relaxed with force convergence 0.001 eV/Å using a conjugate gradient minimization algorithm. A 2×2×2 Monkhorst k-mesh size is used for optimizing the structures. For the energy calculations, the total energy tolerance is set to 0.001 meV. The k-mesh [45] is converged and fixed at 4 × 4 × 4 k-mesh size. The plane wave energy cutoff is set to 600 eV in our calculations. For optical properties, k-point sampling 6 × 6 × 6 and the number of bands 512 have been used which results in convergence of the band gap.

III. RESULTS AND DISCUSSION

A. Validation of functionals

To ensure that our findings are not just an artifact of DFT ϵ_{xc} functionals, different ϵ_{xc} functionals [viz. generalized gradient approximation (PBE) and advanced hybrid functional HSE06] are first thoroughly benchmarked. We find the band gap of MAPbI$_3$ with PBE is 1.54 eV, whereas the experimental band gap is 1.57 eV [12,46]. In Fig. 1(a) we have shown the position of the conduction band minimum (CBm) and valence band maximum (VBM) estimated with different ϵ_{xc} functionals (viz. PBE, PBE+SOC, HSE06+SOC) of

the cubic MAPbI$_3$. From Fig. 1(a), PBE calculation without SOC raises the CBm by 0.88 eV and lowers the VBM by 0.18 eV with respect to PBE+SOC, resulting in a band gap of 1.54 eV, which is in good agreement with the experimental value. In fact, due to this misplaced VBM and CBm levels, local/semilocal functionals perform surprisingly well in estimating the band gap of MAPbX$_3$ (X = I, Br, Cl) [47]. This is why there are many previous works where the SOC effect is completely neglected [32,33,48]. However, SOC effect is significantly important in the electronic structure of MAPbI$_3$ due to the presence of heavy elements (e.g., Pb). Inclusion of SOC degenerates the conduction band levels, which results in splitting of CBm. This further leads to shifting of CBm in the downward direction. Therefore, the obtained band gap with PBE+SOC is 0.48 eV (experimental value ∼1.57 eV [12,46]) [see Fig. 1(a)]. It should be noted here, HSE06 (with the default $\alpha = 0.25$, i.e., by incorporating a 25% of Hartree-Fock exact exchange to capture the electron's self-interaction error) along with SOC is unable to reproduce the experimental band gap. Hence we have calculated the imaginary part of the dielectric function for three values of $\alpha = 0.25$, 0.43 [29], and 0.50. Note that the fundamental gap can be reproduced by the first peak in the absorption spectrum satisfying the optical selection rule [49–51]. We find HSE06+SOC with $\alpha = 0.25$ corresponds to an optical peak at 0.94 eV. However, it is reported that the band gap is 1.50 eV for the tetragonal phase of MAPbI$_3$ [26,29] with $\alpha = 0.43$. This is why we have checked whether the same value of α works for the cubic phase as well. But we obtain a band gap of 1.36 eV corresponding to $\alpha = 0.43$. Therefore, we have further increased the value of α and finally at $\alpha = 0.50$ we have found the theoretical optical peak at 1.53 eV [see Fig. 1(b)]. This is because HSE06 (with $\alpha = 50$%)+SOC results in correct positioning of the VBM by lowering it down, and consequently the experimental band gap is reproduced.

Note that, in the present work, we are more interested in substituting Pb from pristine MAPbI$_3$ to make a composite system viz. MAPb$_{1-X-Y}$Sn$_X$ ⊠$_Y$ I$_3$, where the SOC effect changes as a function of the amount of Pb. Thus even if in the pristine MAPbI$_3$ 50% exact exchange reproduces the correct energetics, a composite system with X substituted Sn atoms and Y Pb-⊠s will for sure not need the same amount of exact exchange. This will also be a complicated function of X, Y and determining this accurately is somewhat impossible without experimental inputs. In view of this, we have performed the rest of calculations with default $\alpha = 0.25$ as in HSE06 with SOC. For sure this may lead to some unprecedented error in the energetics due to over/underestimation of the combined effect of SOC and the electron's self-interaction error to the energetics. However, to estimate formation energies of different conformers with and without defects, we take the difference of total energies. Thus we assume this error elimination (if any) is intrinsically incorporated in taking the differences and the rest of the calculations are therefore justified to be carried out at the level of HSE06 ($\alpha = 0.25$)+SOC.
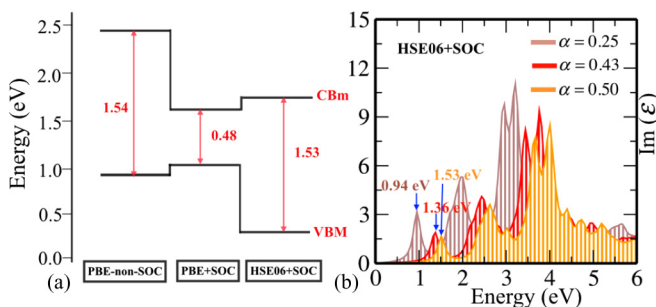

FIG. 1. (a) Band edge alignment using PBE without SOC, PBE + SOC, and HSE06 ($\alpha = 0.50$) + SOC. (b) Calculated absorption spectra using the HSE06+SOC functional for three different values of exact exchange fraction (α): $\alpha = 0.25$ corresponds to peak at 0.94 eV, $\alpha = 0.43$ gives rise to peak at 1.36 eV, and for $\alpha = 0.50$, the peak lies at 1.53 eV.

B. Thermodynamic stability and structural stability

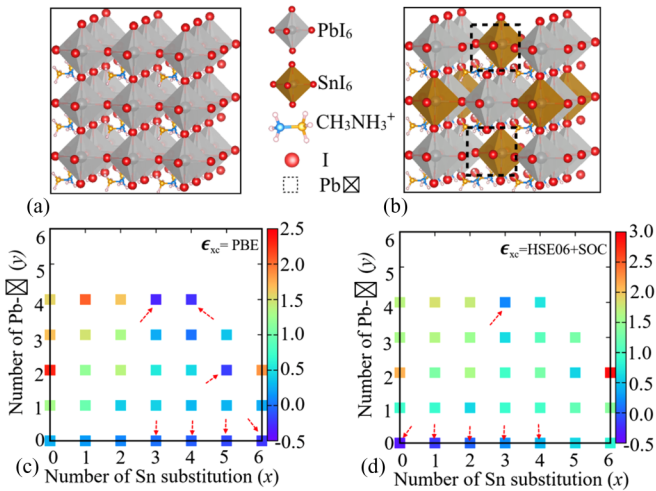Formation energy of the mixed perovskite MAPb$_{1-X-Y}$Sn$_X$ ⊠$_Y$ I$_3$ (for a 2 × 2 × 2 supercell i.e.,

FIG. 2. (a) Relaxed crystal structure of MAPbI$_3$. (b) Crystal structure of Sn substitutions and Pb-⊠s in MAPbI$_3$. Formation energy [$E_f(x, y)$] of different MA$_8$Pb$_{8-x-y}$Sn$_x$⊠$_y$I$_{24}$ structures is represented as a function of Sn substitution and Pb-⊠. The color bar represents $E_f(x, y)$ in eV using ϵ_{xc} (c) PBE and (d) HSE06+SOC. A guide to the eye for the configurations with minimum $E_f(x, y)$ corresponding to each Sn substitution is marked with red arrows.

MA$_8$Pb$_{8-x-y}$Sn$_x$⊠$_y$I$_{24}$) is calculated from the difference of total energies of its precursor materials viz. PbI$_2$, MAI, SnI$_2$, and I$_2$ using the following formula:

$$E_f(x, y) = E(\text{MA}_8\text{Pb}_{8-x-y}\text{Sn}_x ⊠_y \text{I}_{24}) - 8E(\text{MAI})$$
$$- xE(\text{SnI}_2) - (8 - x - y)E(\text{PbI}_2) - yE(\text{I}_2).$$
$$(1)$$

The coefficient of each term on the right-hand side is so chosen that they stoichiometrically balance the number of MA, Pb, Sn, and I atoms in MA$_8$Pb$_{8-x-y}$Sn$_x$⊠$_y$I$_{24}$. In Figs. 2(a) and 2(b) we have shown the relaxed crystal structure of MAPbI$_3$ and doped MAPbI$_3$ (Sn substitutions along with Pb-⊠s).

We have plotted the $E_f(x, y)$ for all possible values of x, y. Here we have employed an iterative strategy [52–54]: At first we have identified energetically the most stable vacancy (substitution) site in the pristine structure, i.e., MA$_8$Pb$_8$I$_{24}$. Following this, we start scanning over all the other remaining seven Pb sites to find out the next stable vacancy (substitution) site and so on. The process is repeated systematically to increase the number of defects in the system (see details in the Supplemental Material [55]). Note that we have shown the thermodynamic stability for PBE and HSE06+SOC ϵ_{xc} in Figs. 2(c) and 2(d). The formation energy values for all the conformers along with literature values [56,57] are given in tabular form in the Supplemental Material [55] (Table S3). However, we have already confirmed that HSE06+SOC will be more accurate for the calculations as it determines the position of the energy bands more accurately. Nevertheless, it is still interesting to verify whether PBE works well, in the context of thermodynamic stability. In Fig. 2(c) with PBE ϵ_{xc} functional, for a given number of Sn substitutions $x = 0$–6, the Pb-⊠s are varied, respectively. The most stable conformers having the lowest formation energy are marked with red

arrows. The pristine system prefers no Pb-⊠s per formula unit when there is no Sn substitution. The introduction of Sn (i.e., $x = 1$–6) with zero Pb-⊠s (i.e., $y = 0$) gradually makes the system energetically stable. For $x = 3$ and 4, the system prefers four Pb-⊠, while for $x = 5$, the system prefers two Pb-⊠s. From the color code we note that as per PBE ϵ_{xc} functional MA$_8$Pb$_0$Sn$_4$⊠$_4$I$_{24}$ and MA$_8$Pb$_1$Sn$_3$⊠$_4$I$_{24}$ are the most stable configurations among all different values of x, y. Following this, HSE06+SOC ϵ_{xc} functional is used to estimate the same of different configurations [see Fig. 2(d)]. Here we have observed that pristine system (i.e., MA$_8$Pb$_8$I$_{24}$ supercell) is the most stable one (inline with experimental observations). However, Sn substitution is also favorable in MAPb$_{1-X-Y}$Sn$_X$⊠$_Y$I$_3$ but up to $0 < X \leqslant 0.5$. Beyond this for $X > 0.5$, the configurations become less stable. On analyzing Figs. 2(c) and 2(d) we conclude that PBE and HSE06+SOC are giving an exactly opposite trend for the thermodynamic stability. For comparison, the thermodynamically stable phases obtained from HSE06 (without SOC) are also given (see the Supplemental Material [55], Fig. S1). We find from Fig. S1 and Fig. 2(d) that the trend of HSE06 and HSE06+SOC are similar despite changes in absolute value of the formation energies. This validates that the SOC definitely plays a crucial role to modulate electronic band energy levels and correct positioning of the CBm, it does not change much the hierarchy of the stability of different configurations. However, the incorporation of the advanced ϵ_{xc} functional is extremely important as the semilocal functional is unable even to give any correct qualitative analysis with respect to HSE06 or HSE06+SOC. Moreover, due to incorrect positions of VBM and CBm (as discussed above), thermodynamic stability of neutral as well as charged defects will be totally wrong using the PBE ϵ_{xc} functional, which is in contrast to the previous studies in literature [26,32,48], where PBE is used to determine the thermodynamic stability.

The stable compositions are then further analyzed to ensure structural stability at operational temperature (i.e., ∼320–350 K). As a first step, the tolerance factor t and octahedral factor μ for all the conformers are determined (see the Supplemental Material [55], Table S1). We have found that among all the thermodynamically stable conformers [as shown in Fig. 2(d)], these conformers viz. MA$_8$Pb$_1$Sn$_3$⊠$_4$I$_{24}$, MA$_8$Pb$_0$Sn$_4$⊠$_4$I$_{24}$ have a tolerance factor and octahedral factor that are not lying within the range of stable cubic perovskite [58,59]. Hence, these conformers are excluded for detailed optical studies to estimate solar cell efficiency. Therefore, to reduce the Pb content from pristine MAPbI$_3$, Sn substitution has more favorable thermodynamic as well as structural stability than Pb-⊠. The thermodynamic stability of Sn substitution is further confirmed from the lower formation energy of charged defects [60] than Pb-⊠ (see the Supplemental Material [55], Fig. S2). In view of this, the most stable phases (MA$_8$Pb$_{8-x}$Sn$_x$I$_{24}$) obtained in terms of thermodynamic stability as well as structural stability (determined from the Goldschmidt tolerance factor, octahedral factor (see Supplemental Material [55], Fig. S3) are taken for further studies. The structural stability of the doped perovskites at 300 K are further confirmed using *ab initio* molecular dynamics (AIMD) simulation (see the Supplemental Material [55], Fig. S4). Note that the structures are thermalized by a
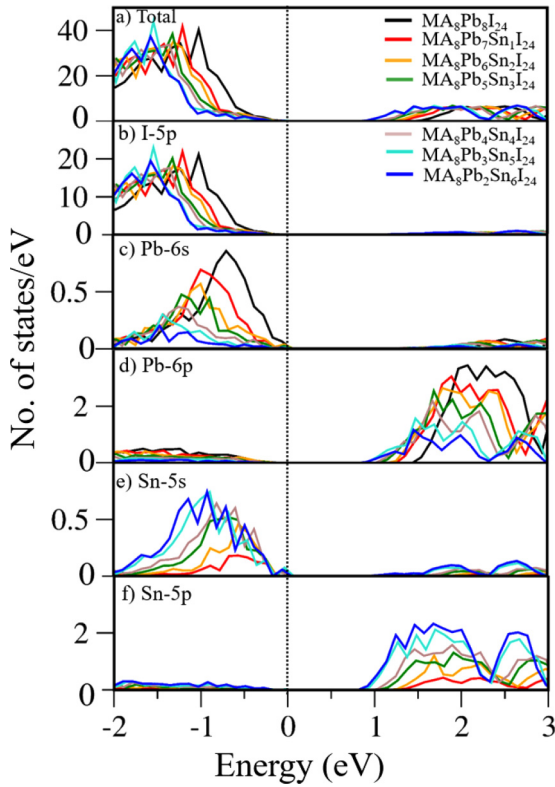
FIG. 3. (a) The total density of states (DOS) of the stable conformers, partial DOS of (b) I-5p orbital, (c) Pb-6s orbital, (d) Pb-6p orbital, (e) Sn-5s orbital, and (f) Sn-5p orbital.

FIG. 4. (a) Imaginary part of a dielectric function, i.e., Im(ϵ), and (b) real part of a dielectric function Re(ϵ) of pristine MAPbI$_3$ and Sn-substituted MAPbI$_3$.

20-ps-long MD simulation run at 300 K with NVT ensemble (Nose-Hoover thermostat) and there are not many changes that are noticed to the ground-state configurations from the radial distribution function plot of the nearest neighbor atoms.

C. Electronic structure and optical properties

Hybrid halide perovskites are considered as the potential candidates in the applications of perovskite solar cells due to their optimum efficiency and high absorption. In order to understand these properties, it is important to get an in-depth insight of the electronic structure of MA$_8$Pb$_{8-x}$Sn$_x$I$_{24}$. To fulfill this purpose, partial density of states (PDOS) are plotted, which indicate the two key features of the origin of strong optical transitions of halide perovskite, (i) p-p/s-p transitions, and (ii) the direct band gap. The results show that, with an increase in concentration of Sn, the electronic states at the upper valence bands (VBs) shifted away from the Fermi level (Fig. 3). On the contrary, near CBm, an increase in percentage of Sn in MAPbI$_3$, results in a shift of CB edges towards the Fermi level as shown in Fig. 3(a). The PDOS shows that the electronic states in the valence band are primarily contributed by the I 5p orbitals mixed with a small component of Pb 6s orbitals, whereas the lower part of the conduction bands are mainly derived from the unoccupied Pb 6p orbitals [Figs. 3(b)–3(d)]. Hence, the strong s-p and p-p couplings [61] pull the lower parts of CBs towards the Fermi level and therefore, results in the reduction of band gap. Thus, with an increase in Sn concentration, the band
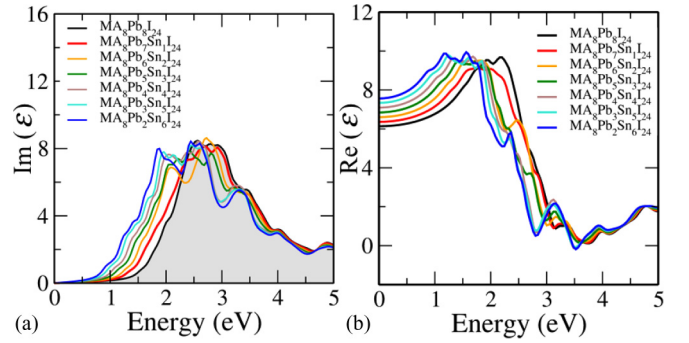
gap is reduced. Since Sn has the same isoelectronic structure as Pb, it shows a very similar contribution in the DOS plot [see Figs. 3(e) and 3(f)]. Therefore, the electronic structure reveals that the reason for strong absorption is the direct p-p and s-p transitions. This motivates us to proceed further and explore the optical properties and theoretical maximum efficiency of these systems.

The optical properties are described by the frequency dependent complex dielectric function $\epsilon(\omega) = \text{Re}(\epsilon) + \text{Im}(\epsilon)$ which represents a linear response of the system to an external electromagnetic field. The imaginary part of the dielectric function is obtained by calculating the interband matrix elements of the momentum operators [62]. The real part can be calculated using Kramer-Kronig transformation. To analyze the optical properties of the MA$_8$Pb$_{8-x}$Sn$_x$I$_{24}$ perovskites, we have calculated the real and imaginary part of the dielectric function of the perovskites in the energy range 0 to 5 eV. The imaginary part of the dielectric function of the conformers MA$_8$Pb$_{8-x}$Sn$_x$I$_{24}$ with Sn concentration $x \in [0, 6]$ shows a redshift towards the infrared region. This behavior is attributed to the gradual reduction of the band gap due to an increase in Sn atoms. The absorption edge increases with an increase in $x \in [0, 6]$ (Sn content) in MA$_8$Pb$_{8-x}$Sn$_x$I$_{24}$ [see Fig. 4(a)]. Similarly, the static value of the real part of the dielectric constant (at $\omega = 0$) increases, with an increase in Sn concentration. This indicates a rise in the static value of the refractive index consecutively with an increase in Sn concentration. The static real part of the dielectric constant Re(ϵ) (at $\omega = 0$) and refractive index of MAPbI$_3$ have been found to be 5.89 and 2.4, respectively, which is well in agreement with the experiment, where refractive index lies in between 2.3–2.6 [63]. Our calculation predicts the peak of Re(ϵ) for MAPbI$_3$ at 2.2 eV, which is in decent agreement with the experimental value of 2.4 eV [64]. From Fig. 4(b) it is clearly observed that peaks are redshifted towards the lower energies in a visible region, causing a rise in Re(ϵ) (at $\omega = 0$), with an increase in Sn content. A large Re(ϵ) (at $\omega = 0$) (static value of dielectric constant) is vital for an efficient solar cell absorber because it provides a high degree of charge screening which can prohibit radiative electron-hole recombination. Therefore, using the Re(ϵ) and Im(ϵ) part of the dielectric function, any optical properties including refractive index (η), extinction coefficient (κ), and absorption coefficient (α) can be calculated using the
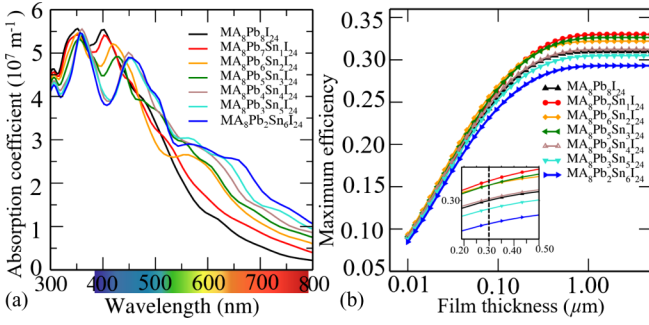
FIG. 5. (a) Absorption coefficient and (b) SLME as a function of film thickness.

TABLE I. SLME at 5 μm absorber layer thickness.

Conformers	SLME (%)
$MA_8Pb_8I_{24}$ ($x = 0$)	31.02
$MA_8Pb_7Sn_1I_{24}$ ($x = 1$)	33.02
$MA_8Pb_6Sn_2I_{24}$ ($x = 2$)	32.21
$MA_8Pb_5Sn_3I_{24}$ ($x = 3$)	32.64
$MA_8Pb_4Sn_4I_{24}$ ($x = 4$)	31.24
$MA_8Pb_3Sn_5I_{24}$ ($x = 5$)	30.49
$MA_8Pb_2Sn_6I_{24}$ ($x = 6$)	29.31

following expressions:

$$\eta = \frac{1}{\sqrt{2}}[\sqrt{\text{Re}(\varepsilon)^2 + \text{Im}(\varepsilon)^2} + \text{Re}(\varepsilon)]^{1/2}, \quad (2)$$

$$\kappa = \frac{1}{\sqrt{2}}[\sqrt{\text{Re}(\varepsilon)^2 + \text{Im}(\varepsilon)^2} - \text{Re}(\varepsilon)]^{1/2}, \quad (3)$$

$$\alpha = \frac{2\omega\kappa}{c}. \quad (4)$$

These types of spectra provide valuable information on optical transition probability corresponding to specific light wavelength. Using Eqs. (3) and (4), the optical absorption coefficients are calculated for $MA_8Pb_{8-x}Sn_xI_{24}$ ($x = 0$–6), which are redshifted and higher than that of undoped MAPbI$_3$ within the visible light region [see Fig. 5(a)]. Note that the absorption spectrum alone cannot find the structure having the highest power conversion efficiency (PCE) for solar cell applications.

D. Spectroscopic limited maximum efficiency (SLME)

To identify and design a highly efficient material for solar cell applications, we need an approach that extends beyond the classical one-dimensional Shockley-Queisser (SQ) criterion [65]. The SQ limit defines the solar cell efficiency on the basis of band gap (direct or indirect) being in the range of 1.0–1.5 eV. This approach does not take into account material dependent absorption spectra and radiative/nonradiative recombination losses, which play an important role in accurately determining the efficiency of the solar cell. Note that for the generation of electron-hole pairs, photons with energy below the energy band gap do not interact with the solar cell. Therefore we can exclude energies below the energy band gap. The improvised multidimensional metric called spectroscopic limited maximum efficiency (SLME) [61,66] depends on absorption coefficient, the nature of band gap, and thickness of the thin film absorber layer. This approach, proposed by Yin *et al.* [61], was based on Fermi golden rule and is very much useful for designing a highly efficient solar cell device. The Fermi golden rule states that the optical absorption of a photonic energy $\hbar\omega$ is directly correlated to

$$\frac{2\pi}{\hbar} \int |\langle v \mid \hat{H} \mid c \rangle|^2 \frac{2}{8\pi^3} \delta[E_c(\vec{k}) - E_v(\vec{k}) - \hbar\omega]d^3k, \quad (5)$$

where $\langle v \mid \hat{H} \mid c \rangle$ is the transition matrix from the states in valence band (v) to the states in conduction band (c) and the integration is performed over the whole reciprocal

space. Using this approach, we have calculated the SLME of $MA_8Pb_{8-x}Sn_xI_{24}$ with a concentration of Sn $x \in [0, 6]$ as a function of the thickness of the absorber layers, as shown in Fig. 5(b). The efficiency curves show that the $MA_8Pb_7Sn_1I_{24}$ structure has the highest power conversion efficiency (33%) (red line), while the $MA_8Pb_2Sn_6I_{24}$ structure has the lowest power conversion efficiency (29.3%) (blue line) among all the considered structures. Therefore, with an increase in Sn concentration up to 50%, the efficiency is reasonably good as compared to pristine. However, the efficiency decreases above 50% Sn concentration. Note that up to 50% Sn concentration, the band gap of the conformers is compatible to be used as an ideal light harvester absorbance (1.1–1.4 eV) [see the Supplemental Material [55] (Table S2)]. The SLME of the conformers $MA_8Pb_{8-x}Sn_xI_{24}$ with Sn content $x \in [0, 6]$ at absorber layer thickness 5 μm is given in Table I. Therefore, it is highly recommended to dope up to 50% Sn, in order to enhance the efficiency of the solar cell, beyond 50% the efficiency of the solar cell degrades. The inset of Fig. 5(b) shows the SLME with a thin 0.3 μm absorber layer. It is interesting to note that the solar cell efficiencies are inline with the thermodynamic stability. We can conclude on the basis of our calculations that the phases which are thermodynamically stable have procured high power conversion efficiency [see Fig. 2(d) and Table I].

IV. CONCLUSIONS

In summary, we have presented an exhaustive and robust study to explore the role of Pb-$\boxtimes$ and Sn substitution in regulating the solar cell efficiency of $MAPb_{1-X-Y}Sn_X \boxtimes_Y I_3$. We have found that the first-principles prediction of thermodynamic stability of inorganic-organic halide perovskite is extremely sensitive to the correct selection of the exchange-correlation functionals, where the choice of HSE06+SOC is indispensable. We find that the most stable configuration is pristine (MAPbI$_3$) itself. However, Sn substitution is also favored up to $0 < X \leqslant 0.5$. Our study further confirms that Pb-$\boxtimes$s are not stable at all. The electronic structure of the stable configurations reveals that the reason for strong absorption is the direct p-p and s-p transition from the valence band predominantly contributed by I $5p$ orbitals and Pb $6s$ orbitals to the conduction band Pb $6p$ orbitals. We have achieved the highest efficiency of 33% for the composite system, and up to 50% Sn substitution, the efficiency is reasonably good as compared to pristine. The lower formation energy, direct p-p/s-p transition, high optical absorption coefficient (redshifted), and maximum solar cell efficiency of the $MAPb_{1-X}Sn_XI_3$

$(0 < X \leqslant 0.5)$ make it a promising candidate for highly efficient perovskite solar cells.

[1] A. Kojima, K. Teshima, Y. Shirai, and T. Miyasaka, J. Am. Chem. Soc. **131**, 6050 (2009).

[2] M. M. Lee, J. Teuscher, T. Miyasaka, T. N. Murakami, and H. J. Snaith, Science **338**, 643 (2012).

[3] M. A. Green, A. Ho-Baillie, and H. J. Snaith, Nat. Photon. **8**, 506 (2014).

[4] M. Gratzel, Nat. Mater. **13**, 838 (2014).

[5] C. Quarti, E. Mosconi, J. M. Ball, V. D'Innocenzo, C. Tao, S. Pathak, H. J. Snaith, A. Petrozza, and F. De Angelis, Energy Environ. Sci. **9**, 155 (2016).

[6] F. Zhang, J. F. Castaneda, S. Chen, W. Wu, M. J. DiNezza, M. Lassise, W. Nie, A. Mohite, Y. Liu, S. Liu *et al.*, Mater. Today (2020), doi: 10.1016/j.mattod.2020.01.001.

[7] J. Qiu, Y. Qiu, K. Yan, M. Zhong, C. Mu, H. Yan, and S. Yang, Nanoscale **5**, 3245 (2013).

[8] N. J. Jeon, J. H. Noh, W. S. Yang, Y. C. Kim, S. Ryu, J. Seo, and S. I. Seok, Nature (London) **517**, 476 (2015).

[9] H.-S. Kim, C.-R. Lee, J.-H. Im, K.-B. Lee, T. Moehl, A. Marchioro, S.-J. Moon, R. Humphry-Baker, J.-H. Yum, J. E. Moser, M. Grätzel, and N.-G. Park, Sci. Rep. **2**, 591 (2012).

[10] W.-J. Yin, T. Shi, and Y. Yan, Appl. Phys. Lett. **104**, 063903 (2014).

[11] Q. Dong, Y. Fang, Y. Shao, P. Mulligan, J. Qiu, L. Cao, and J. Huang, Science **347**, 967 (2015).

[12] C. C. Stoumpos, C. D. Malliakas, and M. G. Kanatzidis, Inorg. Chem. **52**, 9019 (2013).

[13] P. Qin, S. Tanaka, S. Ito, N. Tetreault, K. Manabe, H. Nishino, M. K. Nazeeruddin, and M. Grätzel, Nat. Commun. **5**, 3834 (2014).

[14] N. J. Jeon, H. G. Lee, Y. C. Kim, J. Seo, J. H. Noh, J. Lee, and S. I. Seok, J. Am. Chem. Soc. **136**, 7837 (2014).

[15] W. S. Yang, J. H. Noh, N. J. Jeon, Y. C. Kim, S. Ryu, J. Seo, and S. I. Seok, Science **348**, 1234 (2015).

[16] W. S. Yang, B.-W. Park, E. H. Jung, N. J. Jeon, Y. C. Kim, D. U. Lee, S. S. Shin, J. Seo, E. K. Kim, J. H. Noh *et al.*, Science **356**, 1376 (2017).

[17] M. A. Green, K. Emery, and Y. Hishikawa, Prog. Photovoltaics Res. Appl. **22**, 701 (2014).

[18] G. Abdelmageed, C. Mackeen, K. Hellier, L. Jewell, L. Seymour, M. Tingwald, F. Bridges, J. Z. Zhang, and S. Carter, Sol. Energy Mater. Sol. Cells **174**, 566 (2018).

[19] P.-P. Sun, Q.-S. Li, S. Feng, and Z.-S. Li, Phys. Chem. Chem. Phys. **18**, 14408 (2016).

[20] F. Hao, C. C. Stoumpos, R. P. Chang, and M. G. Kanatzidis, J. Am. Chem. Soc. **136**, 8094 (2014).

[21] Y. Takahashi, R. Obara, Z.-Z. Lin, Y. Takahashi, T. Naito, T. Inabe, S. Ishibashi, and K. Terakura, Dalton Trans. **40**, 5563 (2011).

[22] S. D. Stranks and H. J. Snaith, Nat. Nano. **10**, 391 (2015).

[23] L. A. Frolova, D. V. Anokhin, K. L. Gerasimov, N. N. Dremova, and P. A. Troshin, J. Phys. Chem. Lett. **7**, 4353 (2016).

[24] C. Liu, J. Fan, H. Li, C. Zhang, and Y. Mai, Sci. Rep. **6**, 35705 (2016).

[25] P. Kanhere, S. Chakraborty, C. J. Rupp, R. Ahuja, and Z. Chen, RSC Adv. **5**, 107497 (2015).

[26] D. Yang, W. Ming, H. Shi, L. Zhang, and M.-H. Du, Chem. Mater. **28**, 4349 (2016).

[27] S. X. Tao, X. Cao, and P. A. Bobbert, Sci. Rep. **7**, 14386 (2017).

[28] Q. Wang, Y. Shao, H. Xie, L. Lyu, X. Liu, Y. Gao, and J. Huang, Appl. Phys. Lett. **105**, 163508 (2014).

[29] M.-H. Du, J. Phys. Chem. Lett. **6**, 1461 (2015).

[30] P. Hohenberg and W. Kohn, Phys. Rev. **136**, B864 (1964).

[31] W. Kohn and L. J. Sham, Phys. Rev. **140**, A1133 (1965).

[32] Z.-K. Tang, Z.-F. Xu, D.-Y. Zhang, S.-X. Hu, W.-M. Lau, and L.-M. Liu, Sci. Rep. **7**, 7843 (2017).

[33] Z.-K. Tang, Y.-N. Zhu, Z.-F. Xu, and L.-M. Liu, Phys. Chem. Chem. Phys. **19**, 14955 (2017).

[34] R. Mayengbam, S. Tripathy, and G. Palai, J. Phys. Chem. C **122**, 28245 (2018).

[35] D. Liu, Q. Li, J. Hu, R. Sa, and K. Wu, J. Phys. Chem. C **123**, 12638 (2019).

[36] P. Umari, E. Mosconi, and F. De Angelis, Sci. Rep. **4**, 4467 (2014).

[37] E. Tenuta, C. Zheng, and O. Rubel, Sci. Rep. **6**, 37654 (2016).

[38] Y.-Y. Zhang, S. Chen, P. Xu, H. Xiang, X.-G. Gong, A. Walsh, and S.-H. Wei, Chin. Phys. Lett. **35**, 036104 (2018).

[39] Q. Chen, H. Liu, H.-S. Kim, Y. Liu, M. Yang, N. Yue, G. Ren, K. Zhu, S. Liu, N.-G. Park *et al.*, Phys. Rev. X **6**, 031042 (2016).

[40] J. Heyd, G. E. Scuseria, and M. Ernzerhof, J. Chem. Phys. **124**, 219906 (2006).

[41] J. P. Perdew, K. Burke, and M. Ernzerhof, Phys. Rev. Lett. **78**, 1396 (1997).

[42] P. E. Blöchl, Phys. Rev. B **50**, 17953 (1994).

[43] G. Kresse and J. Furthmüller, Phys. Rev. B **54**, 11169 (1996).

[44] Within the operational temperature range of solar cells (i.e., ~320–350 K), MAPbI$_3$ possesses a cubic phase [67]. Also, Sn introduction is supposed to change the crystallographic phase of the perovskite even at room temperature from tetragonal MAPbI$_3$ to cubic MASnI$_3$ [12]. Thus, in our calculations, we have considered the studied cubic phase of the material.

[45] H. J. Monkhorst and J. D. Pack, Phys. Rev. B **13**, 5188 (1976).

[46] G. E. Eperon, S. D. Stranks, C. Menelaou, M. B. Johnston, L. M. Herz, and H. J. Snaith, Energy Environ. Sci. **7**, 982 (2014).

[47] M. Faghihnasiri, M. Izadifard, and M. E. Ghazi, J. Phys. Chem. C **121**, 27059 (2017).

[48] S. Nagane, D. Ghosh, R. L. Hoye, B. Zhao, S. Ahmad, A. B. Walker, M. S. Islam, S. Ogale, and A. Sadhanala, J. Phys. Chem. C **122**, 5940 (2018).

[49] T. Ahmed, C. La-o-vorakiat, T. Salim, Y. M. Lam, E. E. M. Chia, J.-X. Zhu *et al.*, Europhys. Lett. **108**, 67015 (2015).

[50] B. Zhu, Phys. Rev. B **37**, 4689 (1988).

[51] W. Eberhardt and F. J. Himpsel, Phys. Rev. B **21**, 5572 (1980).

[52] A. Bhattacharya and S. Bhattacharya, Phys. Rev. B **94**, 094305 (2016).

[53] P. Basera, S. Saini, E. Arora, A. Singh, M. Kumar, and S. Bhattacharya, Sci. Rep. **9**, 11427 (2019).

[54] M. Kumar, P. Basera, S. Saini, and S. Bhattacharya, arXiv:1909.09623.

[55] See Supplemental Material at http://link.aps.org/supplemental/10.1103/PhysRevB.101.054108 for supplementary figures, data, and discussion.

[56] A. Senocrate, G. Y. Kim, M. Grätzel, and J. Maier, ACS Energy Lett. **4**, 2859 (2019).

[57] R. Ali, G.-J. Hou, Z.-G. Zhu, Q.-B. Yan, Q.-R. Zheng, and G. Su, Chem. Mater. **30**, 718 (2018).

[58] C. Li, X. Lu, W. Ding, L. Feng, Y. Gao, and Z. Guo, Acta Crystallogr. Sect. B **64**, 702 (2008).

[59] C. Li, K. C. K. Soh, and P. Wu, J. Alloys Compd. **372**, 40 (2004).

[60] C. Freysoldt, B. Grabowski, T. Hickel, J. Neugebauer, G. Kresse, A. Janotti, and C. G. Van de Walle, Rev. Mod. Phys. **86**, 253 (2014).

[61] W.-J. Yin, T. Shi, and Y. Yan, Adv. Mater. **26**, 4653 (2014).

[62] P. Basera, S. Saini, and S. Bhattacharya, J. Mater. Chem. C **7**, 14284 (2019).

[63] P. Löper, M. Stuckelberger, B. Niesen, J. Werner, M. Filipič, S.-J. Moon, J.-H. Yum, M. Topič, S. De Wolf, and C. Ballif, J. Phys. Chem. Lett. **6**, 66 (2014).

[64] D. O. Demchenko, N. Izyumskaya, M. Feneberg, V. Avrutin, Ü. Özgür, R. Goldhahn, and H. Morkoç, Phys. Rev. B **94**, 075206 (2016).

[65] S. Rühle, Solar Energy **130**, 139 (2016).

[66] L. Yu, R. S. Kokenyesi, D. A. Keszler, and A. Zunger, Adv. Energy Mater. **3**, 43 (2013).

[67] M. U. Rothmann, W. Li, Y. Zhu, U. Bach, L. Spiccia, J. Etheridge, and Y.-B. Cheng, Nat. Commun. **8**, 14547 (2017).